January 5, 2016 | vol. 113 | no. 1 | pp. 1–236

PNAS

Proceedings of the National Academy of Sciences of the United States of America www.pnas.org

Arctic tundra methane emissions

Small molecule inhibitor of exocytosis

Genetic protection against dementia

Understanding others' mental states

Dopamine fluctuations and prediction errors

Cold season emissions dominate the Arctic tundra methane budget

Donatella Zona[a,b,1,2], Beniamino Gioli[c,2], Róisín Commane[d], Jakob Lindaas[d], Steven C. Wofsy[d], Charles E. Miller[e], Steven J. Dinardo[e], Sigrid Dengel[f], Colm Sweeney[g,h], Anna Karion[g], Rachel Y.-W. Chang[d,i], John M. Henderson[j], Patrick C. Murphy[a], Jordan P. Goodrich[a], Virginie Moreaux[a], Anna Liljedahl[k,l], Jennifer D. Watts[m], John S. Kimball[m], David A. Lipson[a], and Walter C. Oechel[a,n]

[a]Department of Biology, San Diego State University, San Diego, CA 92182; [b]Department of Animal and Plant Sciences, University of Sheffield, Sheffield S10 2TN, United Kingdom; [c]Institute of Biometeorology, National Research Council, Firenze, 50145, Italy; [d]School of Engineering and Applied Sciences, Harvard University, Cambridge, MA 02138; [e]Jet Propulsion Laboratory, California Institute of Technology, Pasadena, CA 91109-8099; [f]Department of Physics, University of Helsinki, FI-00014 Helsinki, Finland; [g]Cooperative Institute for Research in Environmental Sciences, University of Colorado, Boulder, CO 80304; [h]Earth System Research Laboratory, National Oceanic and Atmospheric Administration, Boulder, CO 80305; [i]Department of Physics and Atmospheric Science, Dalhousie University, Halifax, Nova Scotia, Canada B3H 4R2; [j]Atmospheric and Environmental Research, Inc., Lexington, MA 02421; [k]Water and Environmental Research Center, University of Alaska Fairbanks, Fairbanks, AK 99775-7340; [l]International Arctic Research Center, University of Alaska Fairbanks, Fairbanks, AK 99775-7340; [m]Numerical Terradynamic Simulation Group, College of Forestry & Conservation, The University of Montana, Missoula, MT 59812; and [n]Department of Earth, Environment and Ecosystems, Open University, Milton Keynes, MK7 6AA, United Kingdom

Edited by Mark H. Thiemens, University of California at San Diego, La Jolla, CA, and approved November 17, 2015 (received for review August 12, 2015)

Arctic terrestrial ecosystems are major global sources of methane (CH_4); hence, it is important to understand the seasonal and climatic controls on CH_4 emissions from these systems. Here, we report year-round CH_4 emissions from Alaskan Arctic tundra eddy flux sites and regional fluxes derived from aircraft data. We find that emissions during the cold season (September to May) account for ≥50% of the annual CH_4 flux, with the highest emissions from noninundated upland tundra. A major fraction of cold season emissions occur during the "zero curtain" period, when subsurface soil temperatures are poised near 0 °C. The zero curtain may persist longer than the growing season, and CH_4 emissions are enhanced when the duration is extended by a deep thawed layer as can occur with thick snow cover. Regional scale fluxes of CH_4 derived from aircraft data demonstrate the large spatial extent of late season CH_4 emissions. Scaled to the circumpolar Arctic, cold season fluxes from tundra total 12 ± 5 (95% confidence interval) Tg CH_4 y^{-1}, ∼25% of global emissions from extratropical wetlands, or ∼6% of total global wetland methane emissions. The dominance of late-season emissions, sensitivity to soil environmental conditions, and importance of dry tundra are not currently simulated in most global climate models. Because Arctic warming disproportionally impacts the cold season, our results suggest that higher cold-season CH_4 emissions will result from observed and predicted increases in snow thickness, active layer depth, and soil temperature, representing important positive feedbacks on climate warming.

permafrost | aircraft | fall | winter | warming

Emissions of methane (CH_4) from Arctic terrestrial ecosystems could increase dramatically in response to climate change (1–3), a potentially significant positive feedback on climate warming. High latitudes have warmed at a rate almost two times faster than the Northern Hemisphere mean over the past century, with the most intense warming in the colder seasons (4) [up to 4 °C in winter in 30 y (5)]. Poor understanding of controls on CH_4 emissions outside of the summer season (6–10) represents a large source of uncertainty for the Arctic CH_4 budget. Warmer air temperatures and increased snowfall can potentially increase soil temperatures and deepen the seasonal thawed layer, stimulating CH_4 and CO_2 emissions from the vast stores of labile organic matter in the Arctic (11). The overwhelming majority of prior studies of CH_4 fluxes in the Arctic have been carried out during the summer months (12–15). However, the fall, winter, and spring months represent 70–80% of the year in the Arctic and have been shown to have significant emissions of CO_2 (16–18). The few measurements of CH_4 fluxes in the Arctic that extend into the fall (6, 7, 9, 10) show complex patterns of CH_4 emissions, with a number indicating high fluxes (7, 10). Winter and early spring data appear to be absent in Arctic tundra over continuous permafrost.

Beginning usually in late August or early September, the seasonally thawed active layer (i.e., ∼30–50 cm, near-surface soil layer over the permafrost that thaws during the summer growing season) in the Arctic starts freezing both from the top and the bottom, moving downward from the frozen, often snow-covered soil surface and upward from the permafrost layer (Fig. 1). A significant portion of the active layer can stay unfrozen for months, with temperatures poised near 0 °C because of the large thermal mass and latent heat of fusion of water in wet soils, and for the insulating effects of snow cover and low density surface

Significance

Arctic ecosystems are major global sources of methane. We report that emissions during the cold season (September to May) contribute ≥50% of annual sources of methane from Alaskan tundra, based on fluxes obtained from eddy covariance sites and from regional fluxes calculated from aircraft data. The largest emissions were observed at the driest site (<5% inundation). Emissions of methane in the cold season are linked to the extended "zero curtain" period, where soil temperatures are poised near 0 °C, indicating that total emissions are very sensitive to soil climate and related factors, such as snow depth. The dominance of late season emissions, sensitivity to soil conditions, and importance of dry tundra are not currently simulated in most global climate models.

Author contributions: D.Z., D.A.L., and W.C.O. designed research; D.Z., D.A.L., and W.C.O. performed research; R.C., J.L., S.C.W., C.E.M., S.J.D., C.S., A.K., R.Y.-W.C., and J.M.H. supported the collection and preparation of the Carbon in Arctic Reservoirs Vulnerability Experiment data; J.D.W. and J.S.K. contributed new reagents/analytic tools; D.Z., B.G., P.C.M., J.P.G., V.M., A.L., J.D.W., J.S.K., and W.C.O. analyzed data; R.C., J.L, and S.C.W. analyzed the aircraft data; and D.Z., B.G., R.C., S.C.W., C.E.M., S.J.D., S.D., C.S., A.K., R.Y.-W.C., J.M.H., P.C.M., A.L., J.D.W., J.S.K., D.A.L., and W.C.O. wrote the paper.

The authors declare no conflict of interest.

This article is a PNAS Direct Submission.

Freely available online through the PNAS open access option.

Data deposition: The data reported in this paper have been deposited in the Oak Ridge National Laboratory Distributed Active Archive Center, Oak Ridge data repository (dx.doi.org/10.3334/ORNLDAAC/1300 and dx.doi.org/10.3334/CDIAC/hippo_010).

[1]To whom correspondence should be addressed. Email: dzona@mail.sdsu.edu.

[2]D.Z. and B.G. contributed equally to this work.

This article contains supporting information online at www.pnas.org/lookup/suppl/doi:10.1073/pnas.1516017113/-/DCSupplemental.

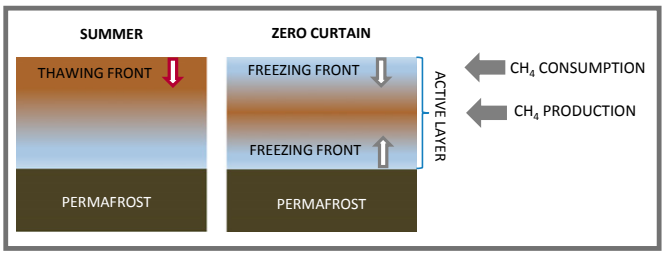

Fig. 1. Diagram of the hypothesized soil physical processes influencing CH_4 production and oxidation depending on the time of the season. We expect that during the zero curtain, the frozen near surface soil layer decreases CH_4 oxidation, resulting in substantial CH_4 emissions, even with lower CH_4 production. Light blue represents cooler soil temperatures, and light brown represents warmer soil temperatures; the arrows point in the direction of the thawing fronts in the summer and freezing front during the cold period.

material. This period has been denoted as the "zero curtain" (19). Soil freezing toward the end of the zero curtain period was considered responsible for sporadic peaks in CH_4 emissions observed in the fall (7, 10), but very sparse data are available to evaluate the importance of fall emissions over a larger scale. The processes influencing CH_4 production and emission in tundra during the cold period (Fig. 1) are not fully explored or understood.

In this paper, we present, to our knowledge, the first year-round eddy flux observations for CH_4 in the Arctic tundra over continuous permafrost to address the critical knowledge gap in cold season CH_4 emissions. Data were obtained from five eddy covariance (EC) towers along a 300-km latitudinal transect on the North Slope of Alaska, with sites extending south from Barrow [Barrow Environmental Observatory (BEO) tower; Biocomplexity Experiment, South (BES) tower; Climate Monitoring and Diagnostics Laboratory (CMDL) tower] to Atqasuk (ATQ) and Ivotuk (IVO) (Fig. 2 and *Materials and Methods*), spanning from June 2013 to January 2015 to capture two summer–fall–winter cycles. We investigated the spatial representativeness of the EC tower data at the regional scale by comparing to CH_4 fluxes estimated from analysis of 15 aircraft flights over the North Slope (2012 to 2014), part of National Aeronautics and Space Administration's Carbon in Arctic Vulnerability Experiment (CARVE). We also examined the correlation between CH_4 concentrations and CO from the High-performance Instrumented Airborne Platform for Environmental Research (HIAPER) Pole-to-Pole Observation (HIPPO) global-scale measurement program to assess whether biological emissions during the cold season measurably influence global distributions of atmospheric CH_4.

Results and Discussion

Site-Level CH_4 Fluxes. Fig. 2 shows continuous eddy flux data for five tundra sites in Alaska: three in Barrow (CMDL, BEO, and BES), one in ATQ, and one in IVO (*Materials and Methods*). Methane emission rates from the cold seasons (September to May) were comparable to (e.g., BEO and ATQ; Fig. 1 *C* and *D*) or higher than (e.g., CMDL; Fig. 1*B*) emissions in summer over a prolonged period. Cumulative emissions for the cold season

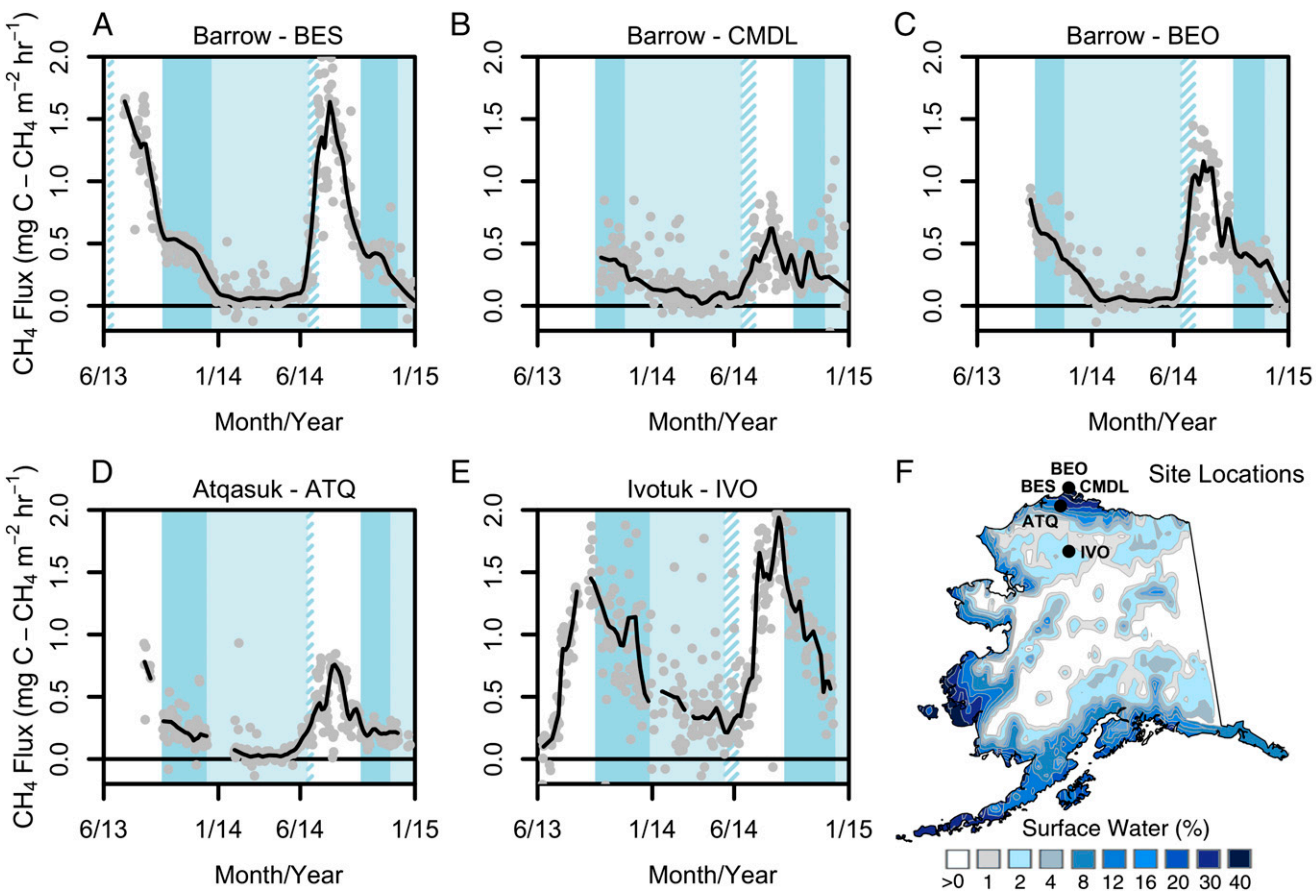

Fig. 2. Methane flux (mg C-CH_4 m^{-2} h^{-1}) measured at the five EC sites on the North Slope, AK: Barrow-BES (*A*), Barrow-BEO (*B*), Barrow-CMDL (*C*), ATQ (*D*), and IVO (*E*) from June 2013 to January 2015 [the gray dots are daily median for a minimum of 24 points per day, and the black line is a 35-d smoothing (lowess) applied to that daily median]. (*F*) Map of Alaska indicating the location of the sites and the percentage of surface inundation (*SI Materials and Methods*). The zero curtain (dark blue), spring thawing with soil temperature around 0 ± 0.75 °C (diagonal hatching) (Fig. S1 and Table S1), summer (no shading), and the balance of the cold season below −0.75 °C (light blue) periods are indicated (*A*–*E*).

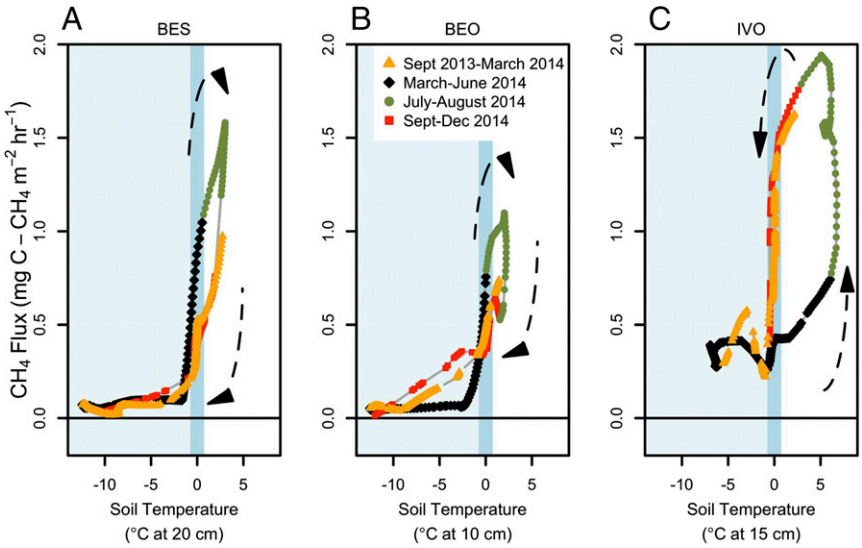

Fig. 3. The methane flux variation with soil temperature on the North Slope of Alaska at Barrow-BES (BES) (*A*), Barrow-BEO (BEO) (*B*), and IVO (*C*) during the indicated periods. The zero curtain period is shaded in dark blue, with soil temperatures below −0.75 °C in lighter blue. The seasonal progression of each phase is indicated by the black arrows. Winter-time data are shown as orange triangles (September 1, 2013 to March 12, 2014) and red squares (September 1, 2014 to December 31, 2014). Data collected during the spring (March 13, 2014 to June, 30, 2014) are shown as black diamonds. Data during the summer period (July 1, 2014 to August 31, 2014) are shown as green circles.

averaged 1.7 ± 0.2 [mean ± confidence interval (CI)] g C-CH_4 m^{-2} at our five sites, accounting on average for 50 ± 9% (mean ± CI) of the annual budget (BES, 37%; BEO, 43%; CMDL, 64%; ATQ, 47%; IVO, 59%). Cold-season emissions dominated the annual CH_4 budget in the driest sites (CMDL, ATQ, IVO), representing a notably higher contribution than previously modeled (6) in other continuous permafrost sites (35%) and also higher than observed year round in boreal Alaska [40%, using periodic sampling of static chambers (20)]. The boreal systems are underlain by discontinuous or sporadic permafrost and are therefore subject to different soil processes than Arctic sites underlain by continuous permafrost (which prevents drainage for extended areas for example).

The highest fall and winter CH_4 fluxes were observed at IVO, an upland tundra site (with a water table below the surface for most of the summer), which had the longest zero curtain period (101 d; Table S1), the warmest soil temperatures during the cold season (Fig. 3 and Fig. S1), the deepest snow depth (*SI Materials and Methods*), and the deepest active layer (Fig. S2 *A* and *B*). Soil temperatures were also poised near 0 °C for more than 90 d at much wetter sites near Barrow (BES). In both cases, the zero curtain period lasted as long as, or longer than, the summer season (Fig. S1 and Table S1). Based on direct measurement of the active layer depth and on soil temperature data, the maximum thaw depth did not begin to decrease appreciably until November or later in all of the sites measured (Fig. S2 *A* and *B*), even though the surface froze in September. During the zero curtain period, we observed strong CH_4 emissions from all five sites, 0.3–2.4 g C-CH_4 m^{-2} (Fig. 2), albeit somewhat lower than the peak summer season CH_4 fluxes observed. The overall contribution of these zero curtain periods to annual emissions was important because of their extended duration (Fig. 2, Fig. S1, and Table S1): emissions of CH_4 during the zero curtain period alone contributed ∼20% of the annual budget (BES, 18%; BEO, 20%; CMDL, 20%; ATQ, 16%; IVO, 32%).

A few previous studies reported measurements of Arctic CH_4 fluxes during the fall (6, 7, 9, 10), but the measurements did not extend to winter and spring. We found that sites with similar summertime CH_4 fluxes had different zero curtain emissions because of different durations and depths of unfrozen soil (Fig. 2 and Fig. S2). For example, summertime cumulative emissions in IVO were 1.9 g C-CH_4 m^{-2} in 2013 and 2.7 g C-CH_4 m^{-2} in 2014, similar to the 2.3 g C-CH_4 m^{-2} (in both years) at BES. However, cumulative CH_4 emissions during the zero curtain were much higher in IVO (2.4 and 2.1 g C-CH_4 m^{-2} in 2013 and 2014, respectively) than BES (0.9 and 0.7 g C-CH_4 m^{-2} in 2013 and 2014, respectively) probably because of interacting effects of greater CH_4 production at IVO, the inhibition of surface oxidation in the fall (Fig. 1), and the deeper thaw depth delaying the complete soil freezing in IVO (Figs. S1 and S2). The emissions of CH_4 produced deeper in the soil continued during the cold season, presumably through cracks and pathways in the near-surface frozen soils (7).

Linear mixed effects modeling (*SI Materials and Methods*) suggested that the depth of the active layer was a critical control on CH_4 fluxes during the summer. The presence of this unfrozen soil layer in the fall and early winter was also a major control on cold season CH_4 emissions; warmer soils resulted in greater CH_4 emission over the entire year. The importance of warm soil temperatures and deep active layer is consistent with the observed higher winter emissions in IVO, where soil temperature at 15 and 30 cm below the surface never dropped below approximately −8 °C compared with at or below −15 °C at the northern sites (e.g., BES and ATQ). The observed CH_4 emissions during fall and winter are consistent with data showing significant microbial populations and metabolic activity at and below 0 °C in the Arctic (16, 21), reflecting the availability of unfrozen water films (22) under these conditions (16). Measurable metabolism has been observed down to −40 °C (23), and CH_4 production has been observed down to −16 °C (21, 24). Soil particles maintain liquid water films until a temperature of at least −10 °C (25), and this unfrozen water can sustain microbial metabolism and greenhouse gas production (26), even as the soil bulk water freezes (25). The direct effect of higher temperature on metabolic activity and the indirect effect of temperature through greater liquid water volume should result in a larger population size and more activity in the methanogenic (i.e., methane-producing) community in the winter at IVO compared with the other, colder, sites. Unfortunately, IVO is the only tower collecting CH_4 fluxes and environmental variables continuously year round over upland tundra at this latitude in Alaska. Therefore, we encourage the establishment of similar upland sites in the Arctic to confirm these observations.

Across all our sites, areas of lower inundation (i.e., less surface area with water table above the surface for most or all of the growing season) had the greatest percentage of total emissions from the cold season, with the highest emissions from IVO with <5% inundation (Fig. 2). In contrast, most modeling studies limit CH_4 emissions to areas with inundated or saturated soils (27). The observed CH_4 emissions that persisted, even when temperatures were well below 0 °C (Fig. 2), present a remarkably

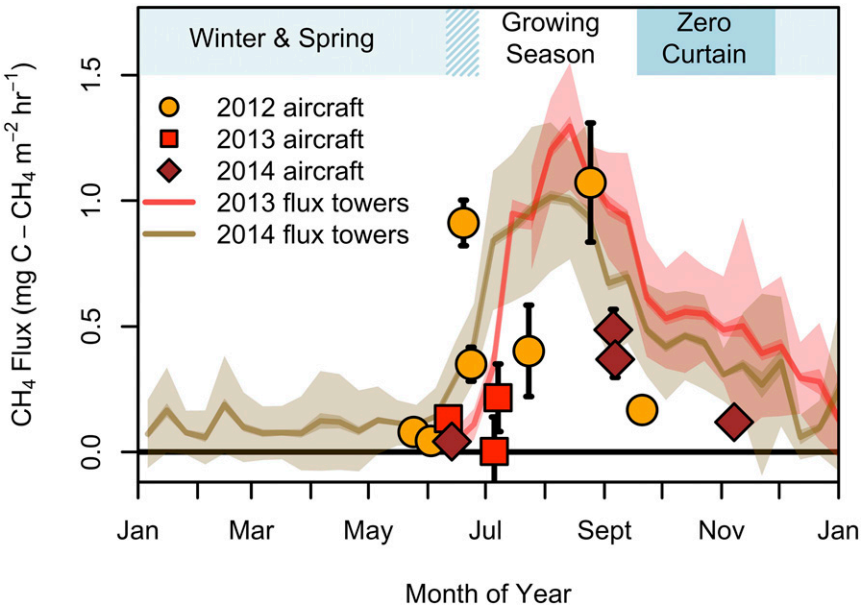

Fig. 4. Ten-day block average of the five EC flux towers over a 300-km transect across the North Slope of Alaska (shaded bands) for 2013 (red) and 2014 (brown), with the mean (solid line), 95% confidence intervals (darker shade), and SD in the CH_4 data (lightest shade). The regional fluxes of CH_4 calculated from the CARVE aircraft data for the North Slope of Alaska are shown for 2012 (yellow circles), 2013 (red squares), and 2014 (brown diamonds). The mean dates for the onset of winter, the growing season, and the zero curtain are indicated in the band on top. Regional scale fluxes of CH_4 (mg C-CH_4 m^{-2} h^{-1}) showed similar seasonal pattern to the EC flux towers across multiple years.

uniform temperature response with a decrease in emission rates as soil temperatures drop (Fig. 3). The fall fluxes show clear relationships with declining soil temperature in the active layer, with little discontinuity in the flux relationship with soil temperature as the soils freeze (Fig. 3). It is likely that freezing of the surface soils decreases near-surface CH_4 oxidation (Fig. 1), maintaining net soil CH_4 emissions even as decreasing soil temperatures results in decreasing CH_4 production rates. At IVO, warmer soil and deeper thaw depth (and therefore greater metabolically active soil volume) resulted in the highest cold season emission rates. This seasonal pattern is very different from that reported by Mastepanov et al. (7, 10), who showed a drop in emissions in late summer/early fall from Greenland tundra, followed by large late-fall CH_4 emissions peaking during complete freezing of the active layer. We instead found fall emissions were persistent until the soil temperatures were well below 0 °C (Fig. 2), with a few instances of sporadic, exceptionally high emissions, e.g., in IVO (Fig. 2) contributing just ~15% of the zero curtain emissions and ~5% of the total annual CH_4 emissions. The underlying sensitivity of CH_4 fluxes to temperature at our sites was, on average, a factor of 2.7 (Fig. 2) for a temperature rise from 0°, to 5 °C, slightly more sensitive than the global mean described by Yvon-Durocher et al. (2).

Spring CH_4 fluxes also increased with increasing active layer temperatures (Fig. 3). The northern sites (e.g., BES and BEO; Fig. 3) showed prompt, steep increases in CH_4 emissions coincident with increasing soil temperatures. The southernmost site (IVO) showed a very different pattern, with apparently much lower temperature sensitivity of net fluxes in the spring vs. fall (Fig. 3). Unlike the wet tundra sites, there is substantial seasonal hysteresis at IVO, likely reflecting a combination of CH_4 oxidation in the spring and summer in the warmer, dry surface layers and CH_4 storage in the deepening, porous active layer. Also, methanogenesis may be stimulated by reduced oxygen in the unfrozen active layer, because the frozen surface (Fig. 1) slows diffusion of oxygen into the soil column (28).

Microbial consumption of CH_4 in the near-surface soil layer (methanotrophy) can be very active in summer (28) but is inhibited by near-surface soil freezing (28, 29). Thus, the fraction of CH_4 escaping to the atmosphere likely increases as the soil surface freezes in the fall. The wettest sites, such as Barrow-BES, where the water table was on average above the surface for the entire measuring period (Fig. S2 *C* and *D*), presumably had low levels of surface oxidation of CH_4. Therefore, this site showed the greatest relative decrease of cold season CH_4 fluxes compared with summer (Fig. 2) because decreasing temperatures reduced CH_4 production, but because oxidation rates were low, there was little benefit from suppression of oxidation in the surface layer in fall.

Our measurements of CH_4 emissions from Arctic tundra are more extensive in both time and space than what have been used to develop and test existing models. Annual CH_4 emissions rates from noninundated Arctic tundra (<20% surface water; Fig. 2) are comparable to those of inundated environments. Most models map CH_4 fluxes to the Arctic landscape using inundation (27), thus dramatically underestimating the emitting area in the Arctic, including during the cold season. The zero curtain interval in fall and winter, and even the period of frozen soils in winter, produce significant, previously underestimated, CH_4 emissions (27). Our work provides the basis for parametric representation of these fluxes and highlights the critical importance of driving models with subsurface soil temperature, and not air temperature.

Regional and Global Scale CH_4 Estimates. Regional CH_4 fluxes calculated from aircraft observations (30) show a strikingly consistent pattern to our eddy flux data (Fig. 4), notably including the persistence of CH_4 emissions into the cold season. The regional aircraft fluxes derived from the CARVE (*Materials and Methods*, *SI Materials and Methods*, and Fig. S3) flights were at times lower than the mean of the EC tower fluxes, as has been observed previously in point-scale and regional-scale flux comparisons (*SI Materials and Methods*). Global-scale measurements (HIPPO; *Materials and Methods*) detected a large enhancement of CH_4 in the Arctic in early November, peaking in the boundary layer of the northern high latitudes (Fig. 5). Because of the flight plans of the HIPPO flights conducted in 2009 to 2011, fluxes

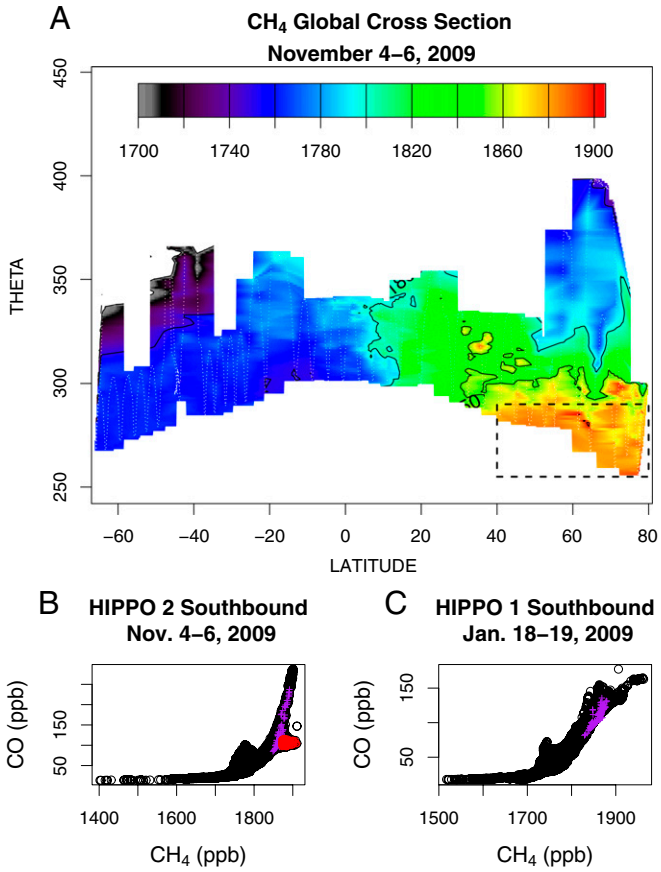

Fig. 5. (*A*) Global cross-section of HIPPO data for CH_4 in the central Pacific and across Alaska (November 4–10, 2009) plotted with potential temperature as the vertical coordinate. The highest CH_4 concentrations are at middle and high latitudes, including the cold, dense air of the high Arctic. (*B*) Methane plotted against CO for the flight data of November 4–10, 2009, showing a subfamily of red points with elevated CH_4 but no corresponding enhancement of CO. (*C*) Same as in *B* but for January 18–25, 2009. In contrast to the November data, elevated CH_4 values are consistently associated with corresponding elevated CO values in January. These results show that elevated CH_4 in November is not associated with anthropogenic CO.

could not be calculated from the HIPPO data. However, the HIPPO data are important to understanding whether the CH_4 fluxes calculated at the flux towers and during CARVE are relevant to CH_4-mixing ratios on the global scale. In the North Slope vicinity (71° N > latitude >65° N), CH_4 is enhanced compared with the global mean, but there is no corresponding elevation of CO, indicating that the CH_4 sources are not associated with transported pollution or fossil fuel burning (Fig. 5*B*; we have only considered CH_4 data between 65° N and 71° N to remove the influence of CH_4 enhancements observed over open leads in sea ice (32)]. By contrast, in January, there were air parcels with high CH_4 consistently associated with CO enhancement, indicating a dominant anthropogenic source of CH_4 compared with the global mean. During this time CH_4 was likely transported from lower latitudes (31). Overall, the HIPPO data are consistent with a substantial biogenic CH_4 source over northern Alaska in fall and with our finding of strong late season biogenic emissions on both a local and regional spatial scale.

Recent estimates using inverse modeling of atmospheric concentration data give CH_4 emissions from Arctic tundra wetlands in the range from 16 ± 5 Tg CH_4 y^{-1} [from CarbonTracker (32)] to 27 (−15 to 68) Tg CH_4 y^{-1} (8). Extrapolating our average CH_4 emissions rates to the Circumpolar Arctic tundra (*SI Materials and Methods*) yields an estimate of 23 ± 8 Tg CH_4 y^{-1} from Arctic tundra, similar to these previous estimates (8, 32). Our estimated CH_4 cold-season emissions as well as those from inverse analysis (27, 32) are significantly higher than that estimated by land-surface models (27, 32). This difference was thought to be linked to anthropogenic emissions, because biogenic emissions were assumed to be negligible during the cold season (27, 32). Overall, the seasonal patterns estimated by models (27) are very different from ours and generally do not include the substantial cold season CH_4 emissions found here. Our finding of large cold-season biogenic emissions from tundra reconciles the atmospheric observations and inverse model estimates without the need to invoke a large pollution influence.

Conclusions

Continued warming and deeper snow are forecast for the future in the Arctic (33). Our results indicate these changes will result in globally significant increases in CH_4 emissions and that cold-season emissions will become increasingly important in this process. Additional year-round CH_4 fluxes and soil climate measurements at sites across the Arctic are urgently needed.

Our results contradict model predictions that simulate and predict the largest CH_4 emissions from inundated landscape. We showed that the largest CH_4 emissions are actually from the site with very low inundation. We believe that the results of our study will impinge directly on our ability to predict future Arctic CH_4 budgets and allow us to revise the variables and processes that must be included to capture the true sensitivity of Arctic CH_4 emissions to climate change.

Materials and Methods

Ecosystem-scale CO_2 and CH_4 fluxes were measured using the EC method with three EC towers in Barrow (9, 15, 34) (CMDL) (71.3225269 N, −156.6091798 W), BEO (71.2810016 N, −156.6123454 W), and BES (71.280881 N, −156.596467 W); one EC tower in ATQ (18) (70.4696228 N, −157.4089471 W); and one EC tower in IVO (68.48649 N, −155.75022 N). The EC towers in CMDL, BEO, BES, and ATQ were upgraded during the summer and fall of 2013 to include closed-path Los Gatos Research (LGR) analyzers [Fast Greenhouse Gas Analyzer (FGGA); LI-7200 (LICOR) (CMDL, ATQ, and IVO); LI-7700 (in IVO in April 2013 and at CMDL in June 2011); a uSonic-3 Class-A (METEK) sonic anemometer (ATQ and IVO); and CSAT-3D (Campbell Scientific) sonic anemometer (BEO, BES, ATQ, and IVO)] which were installed in summer and fall 2013. Fig. S3 displays the regional scale footprint estimates and fluxes from CARVE, Fig. S4 displays the data coverage of the EC CH_4 fluxes for each of the sites, and Fig. S5 displays the comparison between the LI-7700 and LGR. Gap filling of the CH_4 flux data are described in *SI Materials and Methods*, Figs. S6 and S7, and Table S2. To indicate the sites in this study, we used similar names to the ones used in AmeriFlux for ATQ (AmeriFlux site name, US-Atq), for IVO (AmeriFlux site name, US-Ivo), and for BES (AmeriFlux site name, US-Bes) not for Barrow-CMDL (US-Brw) because three sites in Barrow are included in this analysis.

The global-scale measurements were made as part of the HIPPO of Carbon Cycle and Greenhouse Gases Study, flown aboard the National Center for Atmospheric Research (NCAR)-operated HIAPER aircraft. Transects spanned the Pacific from 85° N to 67° S, with vertical profiles every ∼2.2° of latitude during five separate deployments during 2009 to 2011, covering all seasons (35). CH_4-mixing ratios were measured using a midinfrared quantum cascade laser spectrometer (QCLS), developed by Harvard University and Aerodyne Research and operated during HIPPO by the same Harvard team that measured CH_4 during CARVE (30, 36). Common calibration procedures and National Oceanic and Atmospheric Administration (NOAA)-calibrated standards were used during both HIPPO and CARVE, allowing for direct comparison of CH_4-mixing ratios.

ACKNOWLEDGMENTS. We thank the Global Change Research Group at San Diego State University, UMIAQ, Ukpeagvik Inupiat Corporation (UIC), CH2M HILL Polar Services for logistical support; Salvatore Losacco, Owen Hayman, and Herbert Njuabe for help with field data collection; David Beerling for comments on the manuscript; Scot Miller for suggestions on the statistical analysis; and George Burba for suggestions on the data quality assessment. The statistical analysis was performed using R, and we thank the R Developing Core Team. This research was conducted on land owned by the UIC. This

work was funded by the Division of Polar Programs of the National Science Foundation (NSF) (Award 1204263); Carbon in Arctic Reservoirs Vulnerability Experiment (CARVE), an Earth Ventures (EV-1) investigation, under contract with the National Aeronautics and Space Administration; and Department of Energy (DOE) Grant DE-SC005160. Logistical support was funded by the NSF Division of Polar Programs.

1. Kirschke S, et al. (2013) Three decades of global methane sources and sinks. *Nat Geosci* 6(10):813–823.
2. Yvon-Durocher G, et al. (2014) Methane fluxes show consistent temperature dependence across microbial to ecosystem scales. *Nature* 507(7493):488–491.
3. Schuur EAG, et al. (2015) Climate change and the permafrost carbon feedback. *Nature* 520(7546):171–179.
4. Bekryaev RV, Polyakov IV, Alexeev VA (2010) Role of polar amplification in long-term surface air temperature variations and modern Arctic warming. *J Clim* 23(14):3888–3906.
5. Fraser R, Lantz T, Olthof I, Kokelj S, Sims R (2014) Warming-induced shrub expansion and lichen decline in the Western Canadian Arctic. *Ecosystems (N Y)* 17(7):1151–1168.
6. Wille C, Kutzbach L, Sachs T, Wagner D, Pfeiffer E-M (2008) Methane emission from Siberian arctic polygonal tundra: Eddy covariance measurements and modeling. *Glob Change Biol* 14(6):1395–1408.
7. Mastepanov M, et al. (2008) Large tundra methane burst during onset of freezing. *Nature* 456(7222):628–630.
8. McGuire AD, et al. (2012) An assessment of the carbon balance of Arctic tundra: Comparisons among observations, process models, and atmospheric inversions. *Biogeosciences* 9(8):3185–3204.
9. Sturtevant CS, Oechel WC, Zona D, Kim Y, Emerson CE (2012) Soil moisture control over fall season methane flux, Arctic Coastal Plain of Alaska. *Biogeosciences* 9(4):1423–1440.
10. Mastepanov M, et al. (2013) Revisiting factors controlling methane emissions from high-Arctic tundra. *Biogeosciences* 10(11):5139–5158.
11. Hugelius G, et al. (2014) Estimated stocks of circumpolar permafrost carbon with quantified uncertainty ranges and identified data gaps. *Biogeosciences* 11(23):6573–6593.
12. Vourlitis GL, Oechel WC, Hastings SJ, Jenkins MA (1993) A System for Measuring in situ CO_2 and CH_4 Flux in Unmanaged Ecosystems: An Arctic example. *Funct Ecol* 7(3): 369–379.
13. Sachs T, Wille C, Boike J, Kutzbach L (2008) Environmental controls on ecosystem-scale CH_4 emission from polygonal tundra in the Lena River Delta, Siberia. *J Geophys Res Biogeosci* 113(G3):G00A03.
14. Parmentier FJW, et al. (2011) Spatial and temporal dynamics in eddy covariance observations of methane fluxes at a tundra site in northeastern Siberia. *J Geophys Res Biogeosci* 116(G3):G03016.
15. Zona D, et al. (2009) Methane fluxes during the initiation of a large-scale water table manipulation experiment in the Alaskan Arctic tundra. *Global Biogeochem Cycles* 23: GB2013.
16. Monson RK, et al. (2006) Winter forest soil respiration controlled by climate and microbial community composition. *Nature* 439(7077):711–714.
17. Euskirchen ES, Bret-Harte MS, Scott GJ, Edgar C, Shaver GR (2012) Seasonal patterns of carbon dioxide and water fluxes in three representative tundra ecosystems in northern Alaska. *Ecosphere* 3(1):art4.
18. Oechel WC, Laskowski CA, Burba G, Gioli B, Kalhori AAM (2014) Annual patterns and budget of CO_2 flux in an Alaskan arctic tussock tundra ecosystem at Atqasuk, Alaska. *J Geophys Res* 119(3):323–339.
19. Hinkel KM, Paetzold F, Nelson FE, Bockheim JG (2001) Patterns of soil temperature and moisture in the active layer and upper permafrost at Barrow, Alaska: 1993-1999. *Global Planet Change* 29(3–4):293–309.
20. Whalen SC, Reeburgh WS (1988) A methane flux time series for tundra environments. *Global Biogeochem Cycles* 2(4):399–409.
21. Panikov NS, Dedysh SN (2000) Cold season CH_4 and CO_2 emission from boreal peat bogs (West Siberia): Winter fluxes and thaw activation dynamics. *Global Biogeochem Cycles* 14(4):1071–1080.
22. Ostroumov VE, Siegert C (1996) Exobiological aspects of mass transfer in microzones of permafrost deposits. *Adv Space Res* 18(12):79–86.
23. Price PB, Sowers T (2004) Temperature dependence of metabolic rates for microbial growth, maintenance, and survival. *Proc Natl Acad Sci USA* 101(13):4631–4636.
24. Rivkina E, et al. (2004) Microbial life in permafrost. *Adv Space Res* 33(8):1215–1221.
25. Romanovsky VE, Osterkamp TE (2000) Effects of unfrozen water on heat and mass transport processes in the active layer and permafrost. *Permafrost Periglac* 11(3): 219–239.
26. Clein JS, Schimel JP (1995) Microbial activity of tundra and taiga soils at sub-zero temperatures. *Soil Biol Biochem* 27(9):1231–1234.
27. Bohn TJ, et al. (2015) WETCHIMP-WSL: Intercomparison of wetland methane emissions models over West Siberia. *Biogeosciences* 12(11):3321–3349.
28. Yu J, et al. (2007) Enhanced net formations of nitrous oxide and methane underneath the frozen soil in Sanjiang wetland, northeastern China. *J Geophys Res* 112:D07111.
29. Wu X, et al. (2010) Effects of soil moisture and temperature on CO_2 and CH_4 soil atmosphere exchange of various land use/cover types in a semi-arid grassland in Inner Mongolia, China. *Soil Biol Biochem* 42(5):773–787.
30. Chang RY-W, et al. (2014) Methane emissions from Alaska in 2012 from CARVE airborne observations. *Proc Natl Acad Sci USA* 111(47):16694–16699.
31. Sweeney C, et al. (2015) Seasonal climatology of CO2 across North America from aircraft measurements in the NOAA/ESRL Global Greenhouse Gas Reference Network. *J Geophys Res Atmos* 120(10):5155–5190.
32. Bruhwiler L, et al. (2014) CarbonTracker-CH_4: An assimilation system for estimating emissions of atmospheric methane. *Atmos Chem Phys* 14(16):8269–8293.
33. Hay LE, McCabe GJ (2010) Hydrologic effects of climate change in the Yukon River Basin. *Clim Change* 100(3–4):509–523.
34. Zona D, et al. (2012) Increased CO_2 loss from vegetated drained lake tundra ecosystems due to flooding. *Global Biogeochem Cycles* 26(2):GB2004.
35. Wofsy SC (2011) HIAPER Pole-to-Pole Observations (HIPPO): Fine grained, global scale measurements for determining rates for transport, surface emissions, and removal of climatically important atmospheric gases and aerosols. *Philos Trans R Soc Lond A* 369(1943):2073–2086.
36. Kort EA, et al. (2012) Atmospheric observations of Arctic Ocean methane emissions up to 82° north. *Nat Geosci* 5:318–321.
37. Zona D, et al. (2014) Delayed responses of an Arctic ecosystem to an extremely dry summer: Impacts on net ecosystem exchange and vegetation functioning. *Biogeosciences* 11(20):5877–5888.
38. Walker DA, et al. (2005) The Circumpolar Arctic vegetation map. *J Veg Sci* 16(3): 267–282.
39. Vickers D, Mahrt L (1997) Quality control and flux sampling problems for tower and aircraft data. *J Atmos Ocean Technol* 14(3):512–526.
40. Gash JHC, Culf AD (1996) Applying a linear detrend to eddy correlation data in realtime. *Boundary Layer Meteorol* 79(3):301–306.
41. Wilczak J, Oncley S, Stage S (2001) Sonic anemometer tilt correction algorithms. *Boundary Layer Meteorol* 99:127–150.
42. Moncrieff JB, Clement R, Finnigan J, Meyers T (2004) Averaging, detrending and filtering of eddy covariance time series. *Handbook of Micrometeorology: A Guide for Surface Flux Measurements*, eds Lee X, Massman WJ, Law BE (Kluwer, Dordrecht, The Netherlands), pp 7–31.
43. Moncrieff JB, et al. (1997) A system to measure surface fluxes of momentum, sensible heat, water vapour and carbon dioxide. *J Hydrol (Amst)* 188–189:589–611.
44. Ibrom A, Dellwik E, Larsen SE, Pilegaard KIM (2007) On the use of the Webb–Pearman–Leuning theory for closed-path eddy correlation measurements. *Tellus B Chem Phys Meterol* 59(5):937–946.
45. Burba G, et al. (2012) Calculating CO_2 and H_2O eddy covariance fluxes from an enclosed gas analyzer using an instantaneous mixing ratio. *Glob Change Biol* 18(1): 385–399.
46. McDermitt D, et al. (2011) A new low-power, open-path instrument for measuring methane flux by eddy covariance. *Appl Phys B* 102(2):391–405.
47. Horst TW, Lenschow DH (2009) Attenuation of scalar fluxes measured with spatially-displaced sensors. *Boundary Layer Meteorol* 130(2):275–300.
48. Foken T, et al. (2004) Post-field quality control. *Handbook of Micrometeorology: A Guide for Surface Flux Measurements* (Kluwer, Dordrecht, The Netherlands), pp 81–108.
49. Mauder M, Foken T (2006) Impact of post-field data processing on eddy covariance flux estimates and energy balance closure. *Meteorologische Zeitschrift* 15:597–609.
50. Finkelstein PL, Sims PF (2001) Sampling error in eddy correlation flux measurements. *J Geophys Res Atmos* 106(D4):3503–3509.
51. Papale D, et al. (2006) Towards a standardized processing of net ecosystem exchange measured with eddy covariance technique: Algorithms and uncertainty estimation. *Biogeosciences* 3(4):571–583.
52. Hollinger DY, Richardson AD (2005) Uncertainty in eddy covariance measurements and its application to physiological models. *Tree Physiol* 25(7):873–885.
53. Dragoni D, Schmid HP, Grimmond CSB, Loescher HW (2007) Uncertainty of annual net ecosystem productivity estimated using eddy covariance flux measurements. *J Geophys Res Atmos* 112(D17).
54. Papale D, Valentini R (2003) A new assessment of European forests carbon exchanges by eddy fluxes and artificial neural network spatialization. *Glob Change Biol* 9(4): 525–535.
55. Dengel S, et al. (2013) Testing the applicability of neural networks as a gap-filling method using CH_4 flux data from high latitude wetlands. *Biogeosciences* 10(12):8185–8200.
56. Whalen SC, Reeburgh WS (1992) Interannual variations in tundra methane emission: A 4-year time series at fixed sites. *Global Biogeochem Cycles* 6(2):139–159.
57. Gioli B, et al. (2004) Comparison between tower and aircraft-based eddy covariance fluxes in five European regions. *Agric For Meteorol* 127(1–2):1–16.
58. Karion A, et al. (2013) Long-term greenhouse gas measurements from aircraft. *Atmos Meas Tech* 6(3):511–526.
59. Henderson JM, et al. (2015) Atmospheric transport simulations in support of the Carbon in Arctic Reservoirs Vulnerability Experiment (CARVE). *Atmos Chem Phys* 15(8):4093–4116.
60. Nakagawa S, Schielzeth H (2013) A general and simple method for obtaining R^2 from generalized linear mixed-effects models. *Methods Ecol Evol* 4(2):133–142.
61. Johnson PCD (2014) Extension Nakagawa & Schielzeth's R_GLMM^2 to random slopes models. *Methods Ecol Evol* 5:944–946.
62. Du J, et al. (2014) Inter-calibration of satellite passive microwave land observations from AMSR-E and AMSR2 using overlapping FY3B-MWRI sensor measurements. *Remote Sens* 6:8594–8616.
63. Watts JD, Kimball JS, Bartsch A, McDonald KC (2014) Surface water inundation in the boreal-Arctic: Potential impacts on regional methane emissions. *Environ Res Lett* 9(7):1–13.
64. York D, Evensen NM, Martínez ML, De Basabe Delgado J (2004) Unified equations for the slope, intercept, and standard errors of the best straight line. *Am J Phys* 72(3): 367–375.

Supporting Information

Zona et al. 10.1073/pnas.1516017113

SI Materials and Methods

Sites Description. Data for this study were collected from five EC towers across a 300-km latitudinal transect in the North Slope of Alaska. The three northernmost towers (BES, BEO, CMDL) are in the vicinity of Barrow, AK, where mean annual temperature is −11.3 °C and summer precipitation is 72 mm for the 1948 to 2013 period (37). The fourth site, ATQ, is about 100 km south from Barrow. Mean annual temperature and summer precipitation in ATQ are −10.8 °C and 100 mm, respectively, for the 1999 to 2006 period. The most southerly site (IVO) is located near the IVO Airstrip at the foothills of the Brooks Range Mountains, about 300 km south of Barrow, with a mean annual temperature and summer precipitation of −8.9 °C and 210 mm, respectively, for 2003 to 2008. The average snow depth was about 0.3 ± 0.1 m (mean ± SE) in BEO/BES, 0.2 ± 0.2 in ATQ, and 0.4 ± 0.1 in IVO. The vegetation is classified as W1 in Barrow [wet coastal plain dominated by sedges, grasses, and mosses (38)], as W2 in ATQ (tundra dominated by sedges, grasses, mosses, and some dwarf shrubs <40 cm tall), and as G4 in IVO [tussock-sedge dwarf-shrub, moss tundra (38)]. The land-cover types in Barrow and ATQ together are representative of about 60% of all arctic wetlands (38), whereas IVO represents the dominant vegetation type in Alaska. The zero curtain period (19) was defined as the fall period, when the soil temperature at 15- to 20-cm depth (the last soil layer to freeze in our system) was between 0.75 °C and −0.75 °C (Fig. S1 and Table S1). Among the Barrow sites, CMDL presented the least ice-wedge polygon development and is the driest. The presence of low center polygons results in the presence of wet waterlogged ponds interspersed with drier microtopographic features (high center polygons and/or polygons' rims) in the BEO site; BES is located in a vegetated drained lake with restricted drainage, the low topographic results in which being the wettest site.

Environmental Variables. A wide range of meteorological variables were measured at each of the five EC towers, including photosynthetic active radiation (PAR), which was measured with quantum sensors (LI-190; Li-COR) in all sites; net radiation was recorded using a net radiometer [REBS Q7 (Radiation & Energy Balance Systems, Inc.) in BES, BEO, CMDL, and ATQ; and an NR Lite (Kipp & Zonen) in IVO]; incoming solar radiation was measured using pyranometers (CMP3; Kipp & Zonen) in all sites; air temperature and relative humidity (RH) were measured with a Vaisala HMP 45 (in CMDL, BES, BEO, and ATQ), and a Vaisala 155a in IVO (and in BEO after 2013); soil heat flux at −2- to −5-cm depth was measured in four to six locations in all sites with REBS HFT3 (Radiation & Energy Balance); soil temperatures at different depths (at surface −1-, −5, −10-, −20-, and −30-cm depth in BES; at −5, −15, and −30 cm in four profiles in ATQ; and at the surface −5, −15, −30, and −40 cm in four profiles in IVO) were measured with thermocouples (either type-T or type-E; Omega Engineering); soil moisture was measured with a Water Content Reflectometer CS616 (Campbell Scientific) inserted perpendicularly (0–30 cm) or diagonally in different soil layers (0–10 cm and −20/−30 cm) in BES, or horizontally at different depths in the soil (−5, −15, and −30 cm in two different profiles in ATQ; and in three profiles in IVO). More details on these measurements can be found elsewhere (15, 18, 34). Snow depth was measured with Sonic Ranging Sensor in BEO/BES, ATQ, and IVO with an SR50A-L snow senor (Campbell Scientific).

Thaw depth and water table were measured manually during the summer and autumn on a weekly basis in the most accessible sites (BES, BEO, and CMDL) and once every 1–2 months in the more remote sites (ATQ and IVO). A graduated steel rod was used for the thaw-depth measurements, and PVC pipes with holes drilled every centimeter on their sides allowed for the water table measurements (15). Thaw-depth measurements were performed about every 5 m at 45 points in CMDL (three transects of 15 m each in the footprint of the EC tower); at 20 points in BEO, ATQ, and IVO (one transect in the footprint of each EC tower); and at 50 points every 4 m in the footprint of the EC tower at BES. Water table measurements were performed in these same plots for all sites with the exception of CMDL (where the installation of PVC was not allowed).

EC Data Processing and Data Filtering. Half-hourly fluxes were calculated using the EddyPro software (LI-COR), applying the following procedures and corrections: a despiking procedure of fast raw signals (39); the time lag between vertical wind velocity and scalar concentrations was computed based on the maximization of the covariance; turbulent departures from the means were calculated using linear detrending (40); a double-axis rotation and tilt correction was applied according to ref. 41; a correction of the high-pass filtering effect was applied (42); low pass-filtering effect resulting from instrumental attenuations was corrected using different procedures depending on the setup: the analytical method (43) was adopted for the open-path systems (LI-7700); the in situ spectral correction method (44) was used for the closed path (FGGA-24EP) analyzers, more suitable to describe site dependent spectral attenuation along the tubing system. For the closed path and enclosed analyzers (45), the compensation for density fluctuations was not needed as mixing ratio data were measured and used for flux computations (44). For the open-path LI-7700, a spectroscopic correction was computed (46). Spectral correction for instrument separation was applied (47); data quality control (QA/QC) flagging was computed based on stationarity and integral turbulence tests (48, 49), resulting in three flags (0, good; 1, intermediate; 2, poor); random uncertainty attributable to sampling errors was finally estimated following (50). One-point CH_4 storage term was computed based on the concentration measurements of the gas analyzer (51).

To prevent possible biases from the heating system of the METEK in IVO, we modified the activation of the heating of the sonic anemometer to only activate when the data quality was low (as indicated by a quality flag), instead of when temperature was below a set temperature threshold, as commercially available. From September 2014, the CSAT-3D were also externally heated using Freezstop Regular heating cables (Heat Trace), operated at 12 V direct current (DC). These insulated heating lines were cut to length to cover the support arms of the anemometers and yet were far enough removed from the transducer mounting arms to minimize flow distortion and other contamination of wind data. Control of the heating elements was done using the CR3000 data logger and a normally closed solid-state DC relay. The data logger program activated a relay when the sonic transducers were blocked by snow and/or ice, as reported by the diagnostic output by the CSAT-3D. All data when the heating was active were removed for the heated anemometer. Additional data cleaning was performed accordingly to the following criteria: data were removed when the quality flags (48, 49) of H, LE, and CH_4 fluxes were 2; when the internal pressure of the LGR was

≤132 torr (corresponding to malfunctioning of the instrument); or when identified as an outlier (when exceeding a moving-window weekly 1 SD of the individual fluxes).

We used Los Gatos Research FGGA gas analyzers at all sites, except in IVO, where low power availability restricted use to the open-path LI-7700 analyzer. A second LI-7700 was also implemented in CMDL alongside the FGGA to ensure comparability of the results using these two instruments. To this end, in CMDL, we cross-compared the CH_4 fluxes estimated using these two instruments from October 1, 2013 to October 1, 2014 (Fig. S5). The difference between the LICOR and LGR-FGGA-24EP CH_4 fluxes was calculated directly and the resulting distribution used to elucidate features of their uncertainty (Fig. S5). Half-hourly fluxes were used to provide the largest possible sample size. The mean difference (LICOR F_{CH4} – LGR-FGGA-24EP F_{CH4}; ΔF_{CH4}) was −0.0226 mg m^{-2} h^{-1}. Considering that the overall mean values of the LICOR and LGR-FGGA-24EP fluxes were 0.216 and 0.239 mg m^{-2} h^{-1}, respectively, this amounts to about a 10% difference between the two sensors, with the average LICOR flux slightly lower than the LGR-FGGA-24EP. The data were heteroscedastic, whereby the uncertainty estimated from Laplace distributions (Fig. S5) of data binned by flux magnitude increased with the value of the fluxes (52, 53). The average annual data coverage of the CH_4 fluxes (after removal of the data as indicated above) for the entire measuring period was 52% (CMDL LGR), 29% (CMDL LI-7700), 54% (BEO LGR), 58% (BES LGR), 49% (ATQ), and 38% (IVO LI-7700). The seasonal distribution of the data coverage is shown in Fig. S4.

Gap Filling of the Eddy Covariance CH_4 Fluxes. Missing CH_4 flux data were gap-filled by applying artificial neural networks as described in refs. 54 and 55. The following meteorological variables, that most commonly act as drivers for CH_4 emissions, were used following the principle of parsimony and avoiding unnecessary input variables of a cross-correlative and cross-dependent nature: air temperature, air pressure, solar radiation, vapor pressure deficit, soil temperature, soil moisture, and the decomposed wind speed and direction, together with the fuzzy sets representing the annual seasons, as discussed by Dengel et al. (55). A training and a testing dataset for the neural networks were produced, including both daytime and nighttime periods in an equal manner covering all meteorological conditions from both years.

Several combinations of input variables and neurons were tested before we decided to include the same input variables and eight neurons for all datasets to keep the method uniform across all five sites. Each site analysis included 500 repetitions of which the 25 best [correlation coefficient values of the predicted (testing stage) values] runs were included in the gap filling itself. The application of error analysis, the agreement or disagreement between measured and modeled data helped to estimate the overall performance of the neural network models. The overall performance of all five models show no under- or overestimation of the true fluxes. Fig. S6 presents the gap-filled data (red) and the original measurements (gray), and Fig. S7 presents the influence of the gap filling on the daily averaged CH_4 fluxes. Final error analysis results can be found in Table S2, including the correlation of determination (R^2), together with the root mean square error (RMSE) converted to true physical units of mg C-CH_4 m^{-2} h^{-1} indicating the uncertainties of the models.

Circumpolar Arctic CH_4 Emissions Estimates. For their central estimate in the CH_4 emission of Arctic tundra, McGuire et al. (8) used estimated wetland areas of 772,076; 7,540; 18,139; and 812,969 km^2 for North America, North Atlantic, Northern Europe, and Eurasia subregions, respectively, for a total of 1,610,724 km^2; whereas we used the Circumpolar Arctic Vegetation map and included the land cover types B3, B4, G1, G2, G3, G4, P1, P2, S1, S2, W1, W2, and W3, so encompassing all tundra types excluding glaciers and lakes (38), which resulted in a total area of 5,070,000 km^2 across the entire Arctic. Our choice was justified by the importance of upland tundra (e.g., ATQ, CMDL, IVO). The land area we used was greater, but the measured fluxes used were lower than those used by McGuire et al. (8), who included data from boreal wetlands in Alaska (20, 56) in estimating rates of CH_4 emissions. Fortuitously, the differences in land area and fluxes compensated, resulting in similar annual estimates of CH_4 flux to those reported here.

Regional Fluxes (CARVE). The aircraft fluxes were at times lower than the mean of the EC tower fluxes, as has been observed previously in point-scale and regional-scale flux comparisons. The influence of the Brooks Mountain Range has been excluded (Fig. S3 *C* and *F*, gray shading). Additionally, we note that WRF estimates of planetary boundary layer (PBL) ventilation rates are difficult to assess quantitatively and might be subject to particular bias in the fall, when heat fluxes are low. A ∼28% difference of CO_2 eddy fluxes from aircraft compared with towers has been reported (57) and attributed in part to differences in the aircraft and tower footprints. As seen in Fig. S3, the footprint of the regional flux is much larger than that of the flux towers and includes areas assumed to be less productive particularly in autumn and winter, such as frozen lakes. Nevertheless, the regional CH_4 fluxes strongly support the view that our EC fluxes capture relevant cold season CH_4 dynamics and the response of CH_4 emissions to soil climate across the wider North Slope area.

Regional fluxes of CH_4 were estimated with aircraft data from the CARVE 2012 to 2014 (30). CH_4-, CO_2-, and CO-mixing ratios were measured using two independent cavity ring-down spectrometers: one operated wet (58) (G1301-m; Picarro) and one dry (30) (G2401-m; Picarro). Each analyzer was calibrated throughout the flight, ensuring a continuous 5-s time series. Ozone-mixing ratios were measured using a 2B Technologies model 205. The aircraft data were aggregated horizontally every 5 km and vertically in 50-m intervals below 1 km and 100-m intervals above 1 km. Each aggregated position was treated as a receptor in a Lagrangian transport model (WRF-STILT), which calculated the back trajectory of 500 particles from each receptor location. WRF-STILT represents the Stochastic Time-Inverted Lagrangian Transport (STILT) model coupled with meteorology fields from the polar variant of the Weather and Research Forecasting model (WRF) [v3.5.1 (59)]. The WRF-STILT calculation allowed for the quantification of the space and time where upstream surface fluxes influenced the measured mixing ratios. A total 24 h 2D surface influence field (i.e., footprint) was calculated for each flight (e.g., Fig. S3 *C* and *F*), representing the response of the receptor to a unit surface emission (ppb/mg C-CH_4 m^{-2} h^{-1}) of CH_4 in each grid square (0.5° × 0.5° grid). The systematic uncertainty of the calculated surface influence is estimated at 10–20% (59). For comparison with the flux towers, aircraft data were carefully selected and a number of assumptions made to calculate a regional flux of CH_4. Only data collected north of 68° N, west of −153° W, with CO <150 ppb (to remove impacts of anthropogenic influence in the Deadhorse/Prudhoe Bay area), below 1,500 m above ground level and with over 60% surface influence from the North Slope were selected. CH_4 emissions from the higher altitudes of the Brooks Mountain Range were assumed to be negligible (gray area in Fig. S3 *C* and *F*). Assuming a uniform land surface emission, CH_4-mixing ratios should scale linearly with the total land surface influence observed at that receptor point. The flux of CH_4 for each flight day was calculated from the correlation of CH_4 with the STILT land surface influence [ordinary least-square (OLS) regression; Fig. S3 *A* and *D*], where the slope represents the regional flux and the intercept is the regional background CH_4-mixing ratio, which was assumed not to vary greatly during the flight. The

ozone deposition velocity was also calculated in a similar manner (Fig. S3 *B* and *E*), and only flights with an ozone deposition velocity consistent with the expected seasonal cycle were used as a valid CH_4 flux.

Statistical Analysis. To understand the environmental control on CH_4 fluxes over the year, weekly median CH_4 fluxes were modeled as a function of the weekly averaged environmental data. Environmental variables included were soil temperature at 0–5, 10–15, and 20–30 cm; soil water content (SWC) at 0–10 and 20–30 cm; and thaw depth. Only weeks with more than 20 flux and environmental measurements were included in the analysis. Because thaw-depth measurements were collected once a week in the Barrow sites, the weekly average of all available flux and environmental measurements were used in the statistical analyses. The remoteness of the IVO and ATQ sites limited the frequency of visits and therefore of thaw depth measurements. As a result, values were linearly interpolated between measurements during the summer. Because we measured a consistent thaw depth from the end of the summer until October 2014, we assumed a stable depth of the active layer from the end of summer throughout the zero curtain period, and we used the soil temperature profiles and the duration of the zero curtain to extrapolate the thaw depth until soil freezing. After soil freezing, we set the thaw depth to zero until the beginning of the following spring (again defined by the soil temperature profiles, as defined in Table S1). Because CH_4 fluxes presented a skewed distribution, they were log-transformed for all of the statistical analysis. Because of the data loss in the soil environmental data in 2013 and 2014 (e.g., the soil moisture data from IVO and soil temperature data in ATQ), we extended the dataset used for the statistical analysis to include data until May 2015, covering a full year for each site. Only the three sites with the most complete environmental datasets were used in the statistical analysis (ATQ, IVO, and BES).

Linear and nonlinear mixed effects models were used for this analysis (using the lme4 and the nlme in R; R Developing Core Team). The mixed-effects models included the "week" of measurement and "site" as continuous and categorical random effects, respectively, to account for the pseudoreplication and the different sites measured. The nonlinear mixed-effects model was used to test whether an exponential or power fit of soil temperature, and SWC were the best predictor of CH_4 fluxes. However, the increase in the complexity of the model did not justify the use of nonlinear mixed effects modeling, as shown by Akaike information criterion (AIC) values and the partial *F* test of the two models. Therefore, the results of the linear mixed effects models are reported here. The model performance was evaluated based on the AIC values, on the significance of the partial *F* test (used to compare two models), and on the marginal coefficient of determination (similar to the explanatory power of the linear models) for generalized mixed-effects models as output by the r.squaredGLMM function within the MuMIn package in R (60, 61).

The best univariate model explaining the variability in the CH_4 fluxes during the entire year was soil temperature (T) at 20–30 cm, with an AIC of 5.5 and a marginal coefficient of determination of 0.85. During the cold period (from September to May), soil water content at 20- to 30-cm depth was the most important variable explaining CH_4 fluxes, with an AIC of −27 and a marginal coefficient of determination of 0.89. During the summer period, instead, the best univariate model included thaw depth, presenting an AIC of 1.7 and a marginal coefficient of determination of 0.89. The best multivariate model for the CH_4 fluxes during the entire year included soil water content at 20–30 cm in addition to soil T at 20–30 cm, with an AIC of −23 and a marginal coefficient of determination of 0.89. This multivariate model was significantly different in its explanatory power from the univariate model that only included soil T at 20–30 cm (as shown by the significant partial *F* test of the difference in the two models). Similarly, during the cold season, the best multivariate model included soil T at 20–30 cm and soil water content at 20–30 cm, with an AIC of −55 and a coefficient of determination of 0.89 (which was significantly different from the univariate model as shown by the partial *F* test). No multivariate model was statistically different from the univariate one (which only included thaw depth) in the summer.

Surface Inundation at the Tower Sites. Seasonal patterns of aerial proportion (%) of surface water inundation within 25 × 25 km footprints extending over the greater Alaska domain is derived from K-band passive microwave satellite remote-sensing (62, 63). Surface inundation at the tower sites persists from late May following surface thaw through November, when colder air temperatures minimize the presence of liquid water above the soil surface. Wet subsurface soil conditions at ATQ and IVO contribute to peak summer CH_4 emissions of 20–50 mg C-CH_4 m^{-2} d^{-1}, despite lower surface water inundation relative to the CMDL, BES, and BEO tower sites, indicating that substantial CH_4 emissions are not confined to wet, inundated tundra.

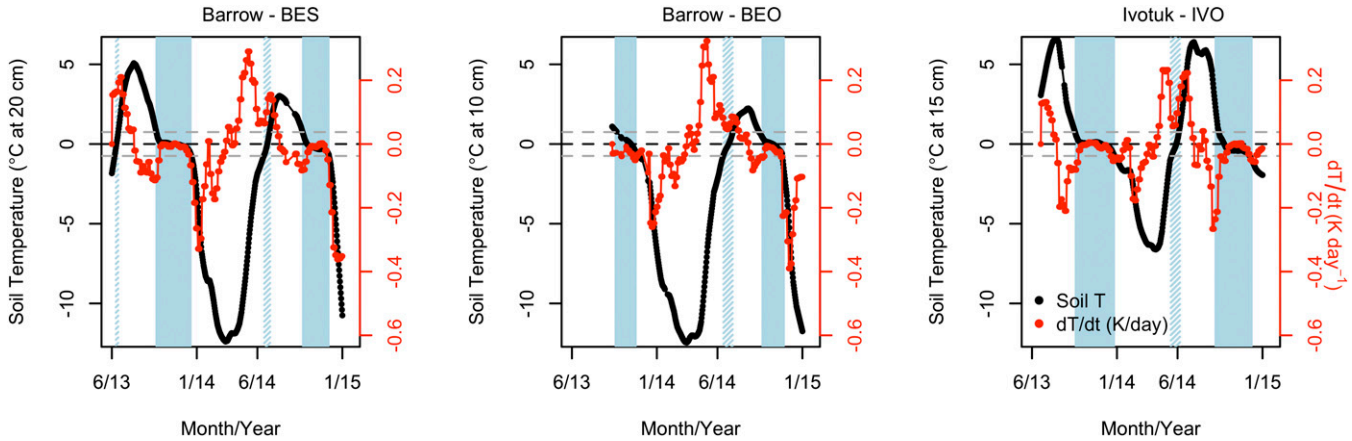

Fig. S1. Zero curtain assessment. Soil temperatures at BES (20 cm, left), BEO (10 cm, center), and IVO (15 cm, right), recorded during 2013 and 2014. The red curves show the time derivative of temperature (°C/d), illustrating the effect of latent heat in stabilizing the temperature when the soils are poised in the zero curtain (0 ± 0.75 °C, light blue shading and horizontal dashed lines). Temperature data have been smoothed using a locally weighted least-squares linear trend ("lowess" filter) with a window of 35 d, roughly equivalent to a two-sided moving average of ±1 wk.

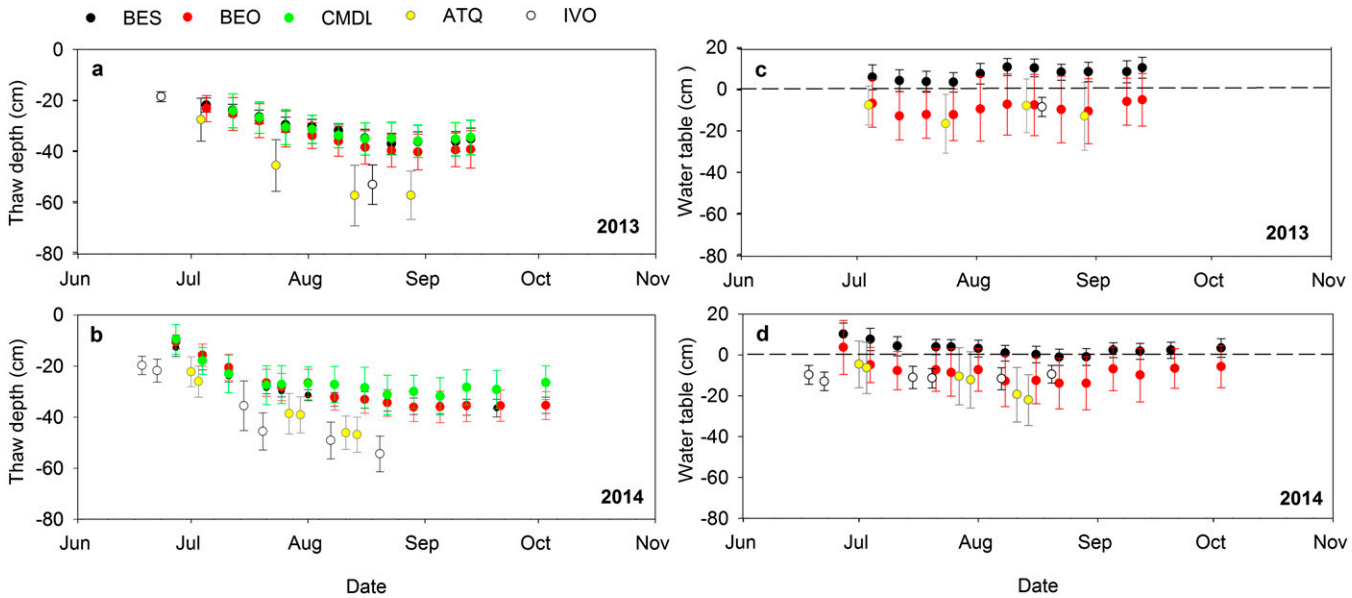

Fig. S2. Thaw depth and water table. Active layer depth (thaw depth) in centimeters from surface (*A* and *B*) and water table (*C* and *D*) depths at four of the five sites during summer and fall 2013 and 2014 (negative values indicate thaw depth and water table below the surface). PVC pipes for water table monitoring were not allowed at the Barrow CMDL site because of clean air restriction by the NOAA. Displayed are averages and SEs from the mean (BEO, ATQ, and IVO: n= 20; CMDL: n= 45; BES: n= 50).

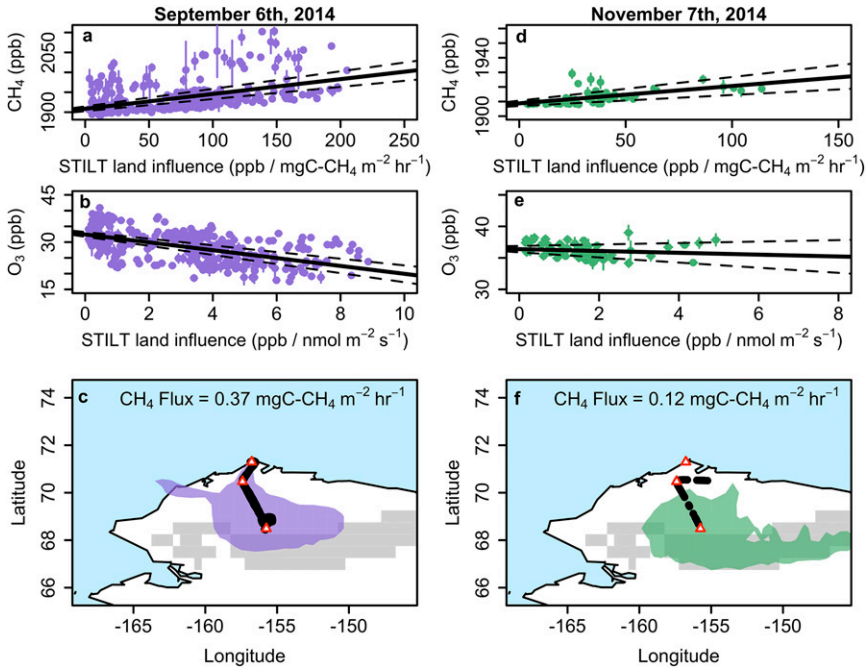

Fig. S3. Methane and ozone aircraft data from CARVE during 2 d in 2014: September 6 and November 7. (*A* and *D*) Correlation of observed CH_4 in ppb on the *y* axis, with the total land influence from the STILT footprint for the matching receptor location on the *x* axis. (*B* and *E*) Correlation of observed O_3 with this same total STILT influence (64). Solid lines show the ordinary least-squares linear regression of these relationships, where the slope of each regression is the calculated flux. (*C* and *F*) Composite footprint for the data used to calculate the flux for each day. Black lines indicate the flight track, and the white triangles with red edges indicate the locations of the eddy flux sites. Gray shading indicates the mountains of the Brooks Range, where fluxes were assumed to be negligible.

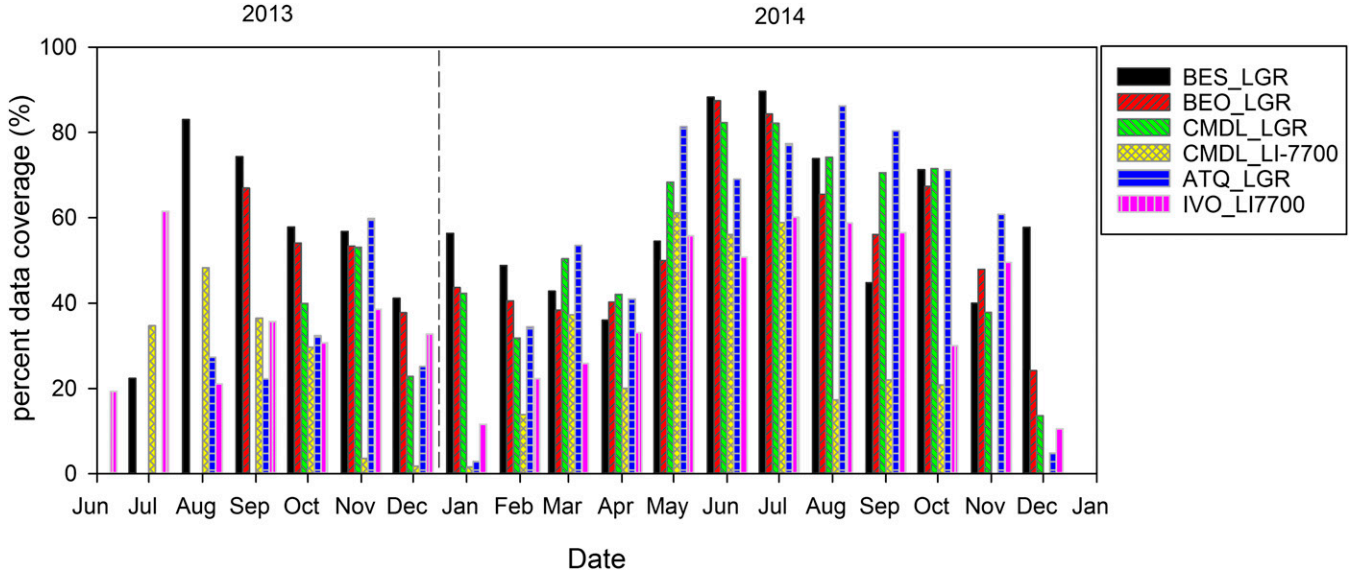

Fig. S4. Percentage of data coverage. Percentage of data coverage at each of the sites of the EC CH_4 fluxes data used in this study.

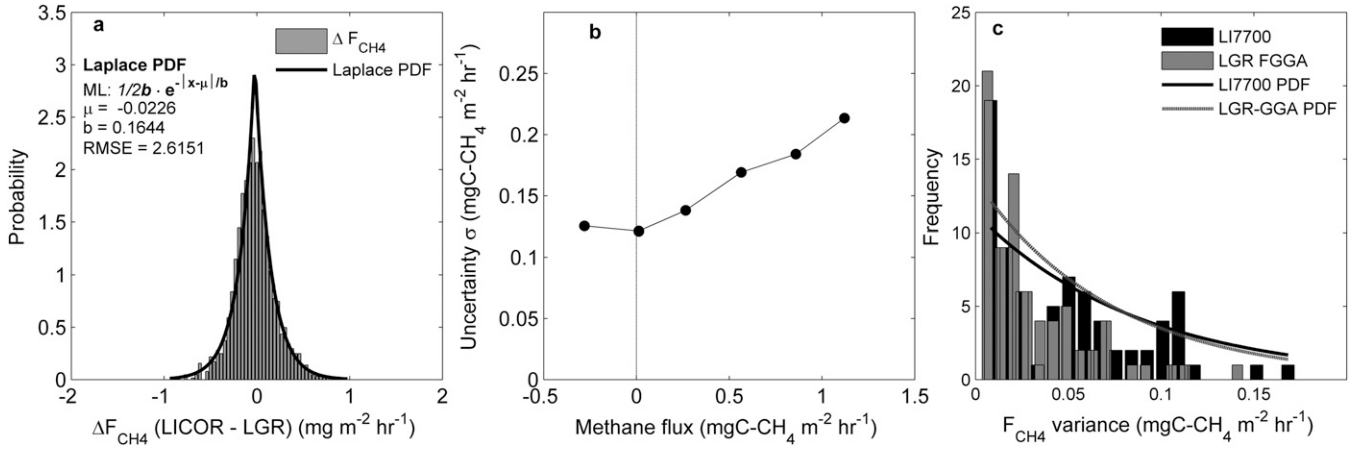

Fig. S5. Comparison of CH_4 fluxes from the LGR-FGGA-24EP and LI-7700 in Barrow (CMDL). (*A*) Differences in CH_4 fluxes derived from the LICOR 7700 and LGR-FGGA-24EP analyzers at CMDL from October 1, 2013 to October 1, 2014 represented by a Laplace probability density function (PDF) (n = 1,681). The histogram and PDF are normalized by trapezoidal integration. The ΔFCH_4 values were calculated as LI-7700 − LGR FGGA-24EP CH_4 fluxes. (*B*) Uncertainty in FCH_4 was binned by flux magnitude. The σ values were calculated as the Laplace analog to SD ($\sqrt{2}$ b). The uncertainty associated with LI-7700– and LGR-FGGA-24EP–derived fluxes increases with the magnitude of the flux (i.e., heteroscedasticity). (*C*) Daily variance in CH_4 fluxes calculated from the LI-7700 and LGR-FGGA-24EP. Fitted lines are exponential PDFs with an estimated μ of 0.087 (95% CI: 0.06–0.14) mg C-CH_4 m^{-2} h^{-1} for the LI-7700 and 0.073 (95% CI: 0.05–0.12) mg C-CH_4 m^{-2} h^{-1} for the LGR-FGGA-24EP.

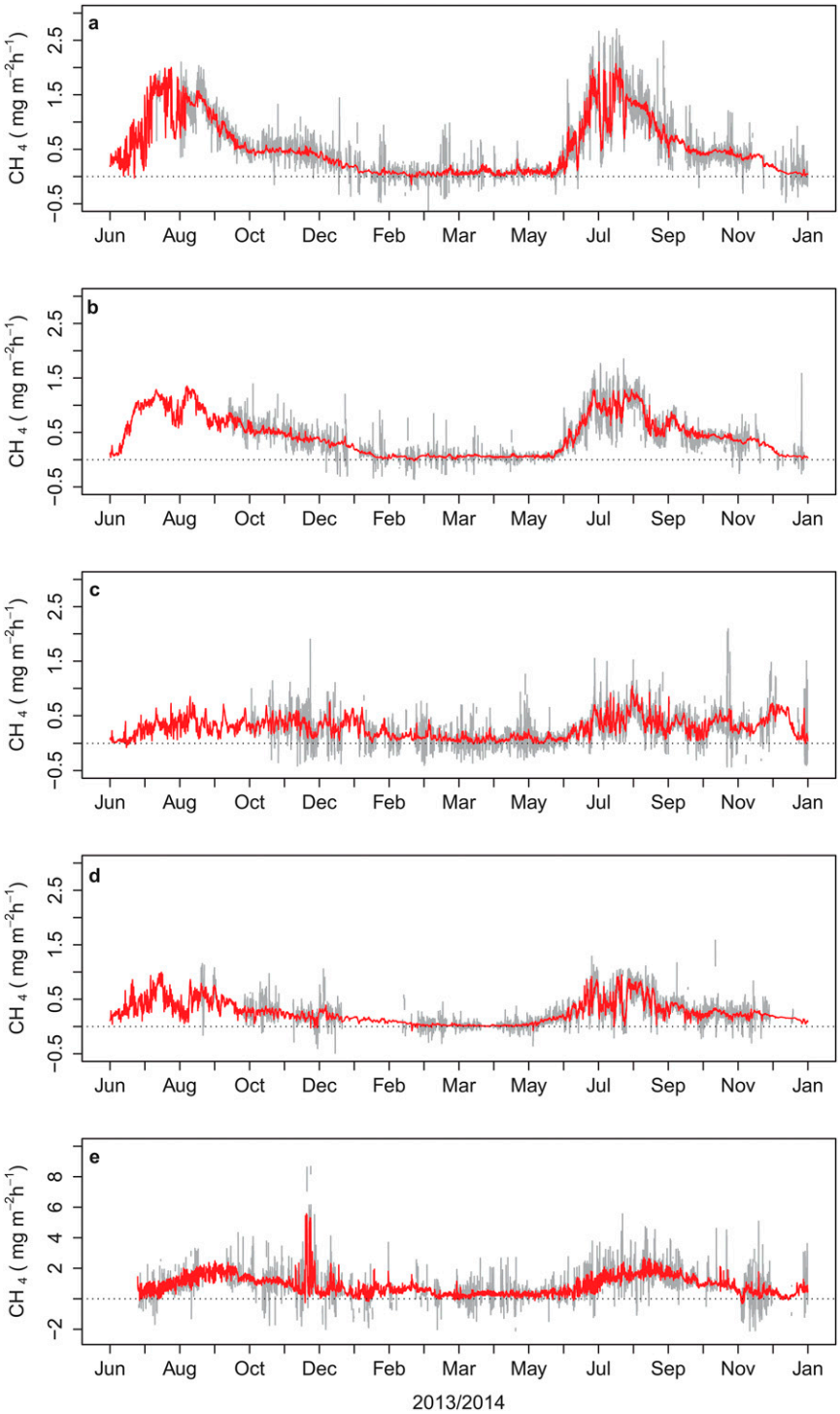

Fig. S6. Gap filling of the methane fluxes. Gap-filled CH_4 fluxes (red) superimposed on the measured fluxes (in gray) for the indicated sites: BES (*A*), BEO (*B*), CMDL (*C*), ATQ (*D*), and IVO (*E*).

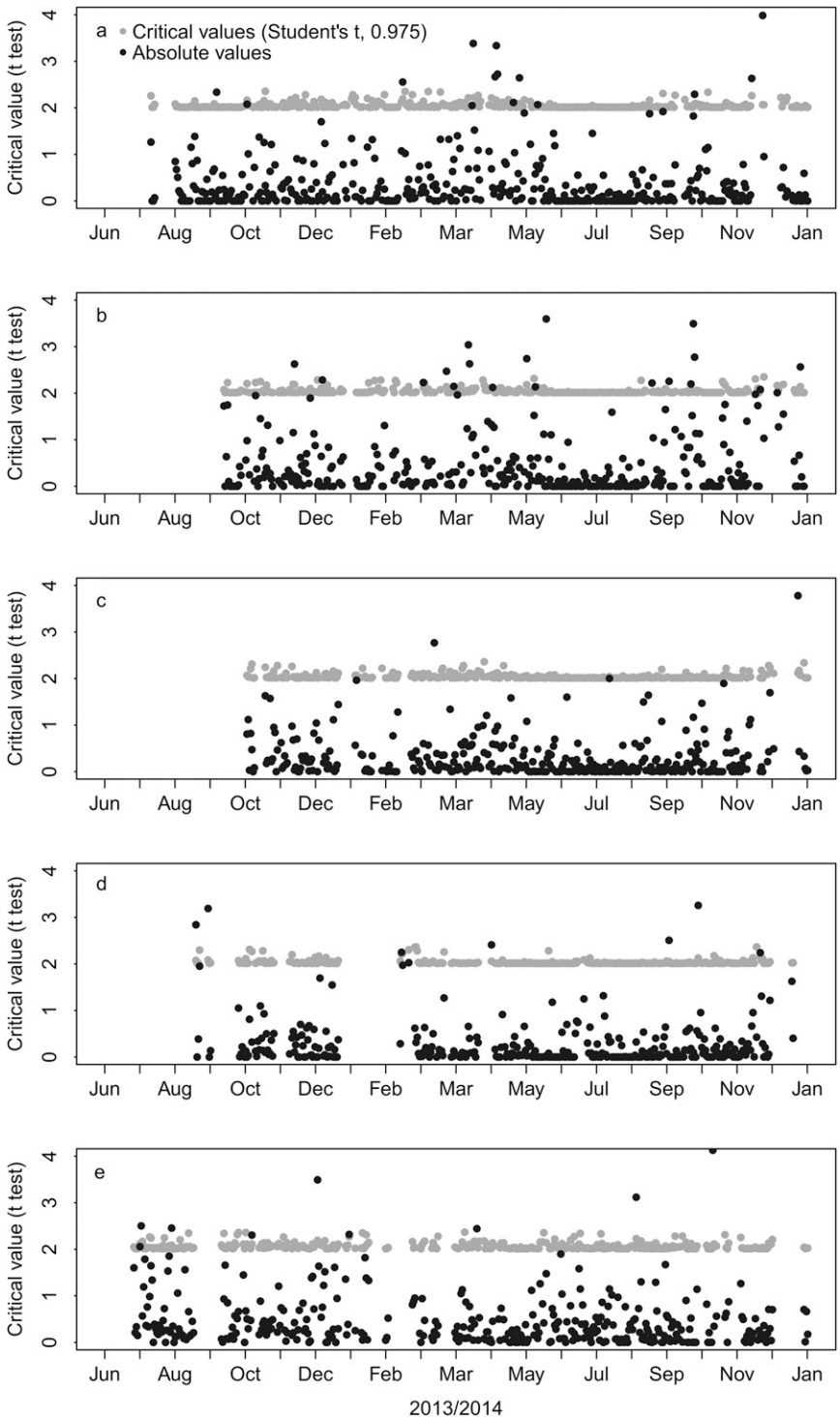

Fig. S7. Critical values of the Student's *t* test distribution of the gap filling for all of the sites. We applied the critical values of the Student's *t* test to each day where more than 6 h of data were available to investigate the influence of the gap filling on the daily averages of CH_4 fluxes: BES (*A*), BEO (*B*), CMDL (*C*), ATQ (*D*), and IVO (*E*). Student's *t* test values higher (black full circles) than the critical values of the Student's *t* distribution (0.975 level) (gray full circles) represent days on which the gap filling of the data had an impact on the final daily average.

Table S1. Zero curtain and spring thawing estimates in 2013 and 2014

Year and site	Spring start	Spring end	Spring thawing days	Autumn start	Autumn end	Zero curtain days	Soil T depth, cm
2013							
BES	—	—	—	261	352	91	20
ATQ	—	—	—	260	343	83	15
BEO	—	—	—	259	314	55	10
IVO	—	—	—	259	360	101	15
CMDL	—	—	—	—	—	—	—
2014							
BES	169	184	15	264	333	69	20
ATQ	154*	174*	20*	264	319	55	15
BEO	167	190	23	262	321	59	10
IVO	135	158	23	245	340	95	15
CMDL	—	—	—	—	—	—	—

Zero curtain dates in the autumn and spring thawing dates and duration are determined from the criteria $-0.75 < T < 0.75$ and are shown in Fig. S1. Because of data loss in the soil temperature data, an average of BES and BEO was used for CMDL. Because spring 2013 was not consistently collected in all sites, we estimated the zero curtain periods starting from autumn 2013. Dashes indicate that no data is available.
*ATQ spring 2013 and autumn 2014.

Table S2. Error analysis of the gap filling of the methane fluxes

Values	BES	BEO	CMDL	ATQ	IVO
Number data points, *n*	8,350	6,978	6,891	6,930	6,309
Data coverage, %	60.0	50.0	49.5	49.8	45.4
Neurons	8	8	8	8	8
Runs	100/500	100/500	100/500	100/500	100/500
Final averaged runs	25	25	25	25	25
Daytime training data coverage, %	49	51	50	49	51
Nighttime training data coverage, %	50	48	49	50	48
Daytime testing data coverage, %	49	50	50	51	49
Nighttime testing data coverage, %	50	49	49	48	50
R^2-training	0.91	0.88	0.61	0.76	0.57
R^2-testing	0.89	0.83	0.52	0.75	0.45
Mean original, true units	0.56	0.41	0.26	0.25	0.89
Mean modeled, true units	0.51	0.43	0.27	0.25	0.86
Mean gap-filled, true units	0.51	0.43	0.27	0.25	0.86
Mean RMSE, true units	0.171	0.15	0.181	0.125	0.69

Error analysis results of the gap filling of the CH_4 fluxes for each of the indicated sites, including the coefficient of determination (R^2) and the RMSE converted to true physical units of mg C-CH_4 m^{-2} h^{-1} indicating the uncertainties of the models.